crystals

MDPI

Review

Thin Films and Glass–Ceramic Composites of Huntite Borates Family: A Brief Review

Elena A. Volkova *, Daniil A. Naprasnikov and Nikolay I. Leonyuk

Department of Crystallography and Crystal Chemistry, Lomonosov Moscow State University, Moscow 119991, Russia; daniilnaprasnikov@mail.ru (D.A.N.); leon@geol.msu.ru (N.I.L.)

* Correspondence: volkova@geol.msu.ru

Received: 18 May 2020; Accepted: 3 June 2020; Published: 6 June 2020

Abstract: Rare-earth aluminum borates, $RAl_3(BO_3)_4$ (where R = Y, Pr–Lu), are of great interest because of their attractive multifunctional properties, depending on their structure and composition. The combination of desirable physical and chemical characteristics makes them promising materials for lasers and nonlinear optics. Research focusing on $RAl_3(BO_3)_4$ (*RAB*) compounds and their solids solutions has continued for more than five decades and has been reflected in numerous articles and several reviews. The last decade's enhanced interest is being conducted towards epitaxial layers because of the availability of other possible applications, for instance, as scintillators, visible emitting phosphors or optical waveguides and waveguide lasers. On the other hand, the tendency of borate melts to form glasses makes them attractive for research of micro-crystallization processes in these systems and can be effortless towards finding relatively inexpensive optical glass–ceramic materials with similar composition as alternative components to laser systems. This article reviews the recent progress carried out hitherto on epitaxial layers and glass–ceramic composites of huntite-type rare-earth aluminum borates.

Keywords: rare-earth aluminum borates; thin film; LPE; YAB; $YAl_3(BO_3)_4$; NAB; $NdAl_3(BO_3)_4$; glass–ceramic composites

1. Introduction

$RAl_3(BO_3)_4$-based materials (hereafter RAB), where R = Y, Pr–Lu, attract considerable attention in the research community due to their attractive physical and chemical properties, such as perfect chemical and mechanical stability, high transparency, high thermal coefficient and, in particular, very high nonlinear optical coefficients. These features make them an ideal matrix for realizing self-doubling diode pumped solid-state lasers. The overall importance of this family of materials is reflected in numerous articles and several reviews that have been published over the years. Even though research focusing on RAB materials has continued for several decades, the abiding interest is fueled by other possible applications, for instance, as scintillators, visible emitting phosphors or optical waveguides and waveguide lasers.

$RAl_3(BO_3)_4$ crystals belong to the large family of double borates with the chemical formula $RM_3(BO_3)_4$, where R is a rare-earth cation (Y, La–Lu) and *M* is a trivalent metal (Al, Sc, Cr, Ga, Fe, Mn). The RAB crystal structure is related to that of the carbonate mineral huntite, $CaMg_3(CO_3)_4$ (space group *R*32) [1,2], where carbon is replaced by boron, calcium by lanthanide element or yttrium and magnesium by aluminum, scandium, chromium, gallium, iron or manganese. Besides, some representatives of the $RM_3(BO_3)_4$ group also have monoclinic modifications (space groups *C*2/*c* and *C*2) depending on the R^{3+} and M^{3+} cations and crystallization conditions (see, for example, Reference [3–7]). The possibility of wide isomorphous substitutions in the R position along with excellent nonlinear optical and lasing properties allow to fabricate a new generation of functional devices based on these materials. YAl-borate, $YAl_3(BO_3)_4$, (hereafter YAB) is the most studied representative

of the RAB group. YAB crystals have been widely investigated as a host matrix for laser applications, with Er^{3+}, Yb^{3+}, Ho^{3+}, Pr^{3+}, Tm^{3+}, Dy^{3+} and Nd^{3+} as the doping ions [8–14]. For example, recently, YAB crystal doped with Er^{3+} or/and Yb^{3+} has been considered as a sufficiently promising material for compact waveguide lasers due to its high efficiency and thermal conductivity [15–18]. Besides bulk crystalline materials, investigations are being conducted towards RAB epitaxial layers. The advantages of thin layer geometry can be exploited in waveguiding structures. However, this approach requires high-quality RAl-borate epilayers with close to perfect interfaces to avoid high propagation losses.

Another promising member in the RAl-orthoborate group is $NdAl_3(BO_3)_4$ (hereafter NAB). NAB is one of the several stoichiometric laser materials which has gained continuous interest due to its suitability for miniature laser action. NAB solids exhibit such features as a low laser threshold, a high gain, a linearly polarized output and a small beam divergence. This material is characterized by the highest Nd^{3+} concentration (5.43×10^{21} cm^{-3}) among all currently known self-activated laser crystals [19]. Continuous-wave laser gain experiments have shown that NAB is quite attractive for microchip diode-pumped solid-state lasers [20]. NdAl-borate demonstrates a much lower concentration quenching of the fluorescence lifetime in comparison with conventional hosts such as Nd:YAG [3,21]. Weak concentration quenching, as well as related properties of other $RM_3(BO_3)_4$ solids, appear as a result of crystal structure features. Regardless of the NAB modification, the Nd^{3+} ions occupy only regular lattice sites well-shielded from one another by Al^{3+} ions and connected to each other by means of Nd–O–Al–O–Nd interactions. The distance between two nearby Nd^{3+} ions is found to be 5.9 Å. Thus, Nd–Nd cross-relaxation is minimized despite the high Nd concentration. Additionally, NAB hardness is comparable to that of YAl-garnet crystal [19]. Another unsolved problem concerns the determination of growth parameters for NAB polymorphous modifications. Hong and Dwight first defined the crystal structure of NdAl-borate almost half a century ago [3]. Later, it was established that $NdAl_3(BO_3)_4$ exhibits three polymorphic modifications: rhombohedral *R32* and two monoclinic with the *C2*/*c* and *C2* space groups for low- and high-temperature forms, respectively [6,22,23]. Currently, structural aspects of $NdAl_3(BO_3)_4$ are still the subject of discussions in the literature. Although Hong and Dwight [3] provided the data for a low-temperature *R32* modification and described its crystal structure, Lutz and Huber [22] reported the existence of two monoclinic forms only. As it is mentioned in Reference [23], the appearance of a rhombohedral modification depends on both the temperature and supersaturation of the fluxed melt and quantitative proportions of the co-crystallizing phases of $KNd(MoO_4)_2$ and $NdAl_{2.07}(B_4O_{10})_{0.6}$. A slight change in one of the above parameters leads to the appearance of a monoclinic modification. Calculations of the second-order optical nonlinearity in trigonal NdAl-borate were performed. As a result, it was shown that $NdAl_3(BO_3)_4$ is also a self-frequency-doubling laser crystal with a high nonlinear coefficient $d_{11} = -5.8 \times 10^{-9}$ esu [21]. However, there are several difficulties in the growth of high-quality NAB bulk crystals from flux melts. Thus, epitaxial layers growth may partially solve the problem of low crystal quality.

As RAl-borates melt incongruently, growth from high-temperature solutions is the only suitable technique for fabrication of RAB bulk crystals. Liquid-phase epitaxy (LPE) seems to be the most suitable method to fabricate crystalline epilayers of rare-earth aluminum borates. Moreover, the growth of bulk borate crystals from molten solutions with high optical quality and sufficient sizes for technological applications is a relatively expensive process.

The last decade has seen dynamic development in the field of the synthesis and characterization of nanocrystals and transparent glass–ceramic (GC) materials. In this connection, crystals with an ordered structure are precipitated in the glasses for manufacturing optoelectronic devices. Then, because of controlled heat treatment, it is possible to obtain GCs with nanocrystals in a glass matrix [24]. The tendency of borate melts to form glasses makes them attractive for research of micro-crystallization processes in these systems and can be effortless towards finding relatively inexpensive optical glass–ceramic materials with similar composition as alternative components to laser systems.

The paper presents a brief synthesis and characterization of epitaxial layers and glass–ceramic composites of huntite-type rare-earth aluminum borates.

2. Thin Film Growth

The growth of large area RAB crystals with high optical quality is important both for material science and further technological applications. Besides the well-established procedure for the growth of pure and doped RAB bulk crystals from a high-temperature solution on dipped seeds, only a few references regarding the growth of thin films with a huntite-type structure could be found in the literature. Since rare-earth aluminum borates melt incongruently when heated in air [8], their crystals cannot be obtained by the melt technique. Thus, thin film growth of $RAl_3(BO_3)_4$ is accomplished by three methods, viz., the liquid-phase epitaxy technique, polymeric precursor (PP) and sol–gel methods (SG).

2.1. Liquid-Phase Epitaxy Technique

LPE is a high-temperature solution growth technique consisting of the material that will be grown from a suitable solvent on a flat oriented single crystal substrate. Thus, many principles, choice of the flux and technological experiences can be transferred to LPE from the growth of bulk crystals [25]. Liquid-phase epitaxy is not a new technology. It was used for preparing epitaxial layers of semiconductor materials until it was replaced by molecular beam epitaxy and metal-organic vapor phase epitaxy techniques. LPE growth was firstly introduced for III–V compounds by Nelson in 1963 [26]. Since the supersaturation during epitaxy is low enough and occurs near the thermodynamic equilibrium, LPE allows to fabricate high-quality single crystal layers. Nowadays, epitaxial growth from the vapor phase is widely used for the industrial growth of semiconductors' thin layers. Nevertheless, LPE is almost the only suitable method for the growth of oxide materials with a complex structure. The LPE growth technique was applied to the fabrication of yttrium iron garnet films by Linares back in 1968 [27]. The first LPE experiments on transparent optical materials demonstrate that high-quality single crystals' epilayers can be grown for waveguides, amplifiers, lasers and so on. This has led to intense investigations of the fundamental and experimental aspects of LPE of oxide compounds.

2.1.1. Key Parameters of LPE

For the achievement of high-quality film perfection, three key parameters have to be satisfied: lattice misfit, relative supercooling/supersaturation and substrate misorientation.

The lattice misfit describes the difference between the structural and thermal characteristics of the substrate and the epitaxial layer. Its value at a certain temperature can be calculated according to the equation

$$f_{latt} = (a_{layer} - a_{sub})/a_{sub} \quad (1)$$

where a_{layer} and a_{sub} are the lattice parameters of the grown layer and substrates at a given temperature, respectively.

Homoepitaxy represents the best choice as it usually leads to an excellent lattice matching, identical melting temperatures, thermal expansion coefficients, composition and so on. In the case of ideal homoepitaxy, the lattice misfit is zero. Nevertheless, it is not a suitable method, in particular, for waveguide fabrication. A planar waveguide consists of thin layers of optically transparent media with a higher refractive index than the adjacent substrate. Co-doping the active layer with suitable fractions of R^{3+} cations allows to provide the necessary refractive index contrast [28]. The choice of dopant concentration is also governed by the requirements of good lattice matching in order to avoid structural stress, dislocations and stacking faults.

Lattice constants of the growing layer depend on the type and concentration of the doping cations. Their values along the crystallographic axes can be found using Vegard's law [29]. For instance, for rhombohedral Er, Yb-codoped YAB layers, they can be expressed as

$$a_{layer} = x \times a_{ErAB} + y \times a_{YbAB}\ x + (1\text{-}x\text{-}y) \times a_{YAB}$$

$$c_{layer} = x \times c_{ErAB} + y \times c_{YbAB}\ x + (1\text{-}x\text{-}y) \times c_{YAB}$$

where a_{ErAB}/c_{ErAB}, a_{YbAB}/c_{YbAB} and a_{YAB}/c_{YAB} are the lattice constants at a certain temperature for ErAB, YbAB and YAB, respectively, and x and y are the molar fractions of R cations with respect to Y in yttrium-aluminum borate.

Lattice parameters of both the substrate and active layer also depend on temperature according to the thermal expansion equation

$$\Delta a = a_{T_2} - a_{T_1} = a_{T_1}\alpha(T_2 - T_1) \quad (2)$$

where a_{T_1} and a_{T_2} are lattice constants at temperatures T_1 and T_2 respectively, and α is the linear thermal expansion coefficient.

The layer quality at LPE greatly depends on the growth temperature T_g and supersaturation of the flux melt. The relative supersaturation is defined as

$$\sigma = (c\text{-}c_0)/c_0, \quad (3)$$

where c and c_0 represent the actual and equilibrium concentration of the solute at a given temperature.

It is not easy to measure the equilibrium concentration experimentally, but it can be calculated from the data on solubility for bulk crystals of the same composition. Besides σ, the supersaturation can be expressed via supercooling ΔT:

$$\Delta T = T_s - T_g, \quad (4)$$

where T_s and T_g are the saturation and growth temperatures for a certain solute concentration. A high ΔT value leads to high growth rates, so some defects occur in the layer. Most commonly occurring defects are inclusions of mother solutions and the appearance of microcrystals of the growing phase on the substrate.

The substrate misorientation is an angular deviation of the substrate surface from a certain crystallographic plane. Large misorientation suppresses surface nucleation, providing steps and kinks and changing the mechanism of epitaxial layer development. Epilayers obtained on substrates with large misorientation angles demonstrate the step-bunching process with very small interstep distances. Thus, the layer surface becomes rough which is not suitable for most applications. The misorientation of available substrates greatly depends on the precise orientation and following polishing. Based on the analysis of the literature data on LPE growth of oxide compounds, the desirable orientation of borate substrates should be ≤ 0.1°.

2.1.2. LPE of Rare-Earth Layers with Huntite-Type Structure

The first LPE experiments on RAl-borates were presented in 1979 [30]. $NdAl_3(BO_3)_4$ epilayers of 50 μm thickness oriented parallel to the *a* plane were obtained on as-grown $Gd_{0.59}La_{0.41}Al_3(BO_3)_4$ crystals (Figure 1). The NAB layers were grown from PbO-PbF_2 flux melt by the dipping method in the temperature range of 950–970 °C during less than 4 h. The growth rate of the layer was 1 μm/min. Their absorption and luminescence characteristics were identical with those for NAB bulk laser crystals.

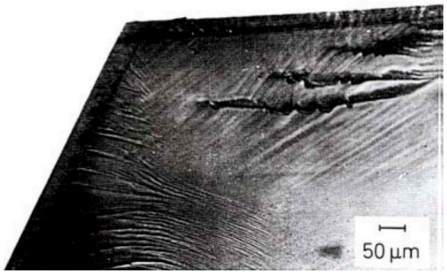

Figure 1. $NdAl_3(BO_3)_4$ epitaxial layers of 50 μm thickness on $Gd_{0.59}La_{0.41}Al_3(BO_3)_4$ substrate [30]. Reprinted from the Journal of Crystal Growth, 47, Lutz F., Leiss M., Müller J., Epitaxy of $NdAl_3(BO_3)_4$ for thin film miniature lasers, 130–132, Copyright (1979), with permission from Elsevier.

Later Lutz et al. reported the growth of $NdGa_{2.79}Cr_{0.03}(BO_3)_4$ layers by isothermal LPE with axial rotation [31]. The substrates were $Gd_{0.59}La_{0.41}Ga_3(BO_3)_4$ single crystals of 4 mm long and 1 mm in diameter grown from a Li_2O-B_3O_3 flux. The LPE experiments were carried out from the melt of an $NdGa_{2.97}Cr_{0.03}(BO_3)_4$ composition with an excess of B_2O_3 using PbO-PbF_2 flux in the temperature interval 920–970 °C. The authors varied the dipping time t in the range 15–90 min and rotation frequency ν from 0 to 100 min^{-1}. The best layer quality was achieved at T = 940 °C and ν = 50 min^{-1}. Epitaxy results were interpreted from the point of view of growth kinetics (Figure 2). The relations obtained within LPE were compared with the growth model of Ghez and Giess [32,33], which imply a two-step crystallization process with diffusion of the crystal components and their incorporation into the layer.

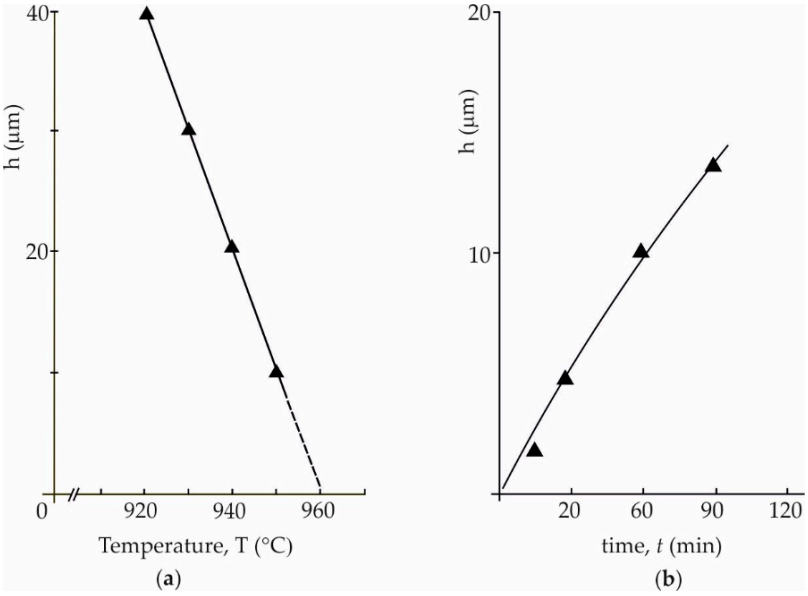

Figure 2. The thickness of the $NdGa_{2.97}Cr_{0.03}(BO_3)_4$ epilayer: (**a**) vs. growth temperature (t = 60 min, ν = 27.3 min^{-1}); (**b**) vs. growth time (T = 950°C, ν = 27.3 min^{-1}) [31]. Reprinted from the Journal of Crystal Growth, 48, Lutz F., Rüppel D., Leiss M., Epitaxial layers of the laser material $Nd(Ga,Cr)_3(BO_3)_4$, 41–44, Copyright (1980), with permission from Elsevier.

The resulting lattice mismatch of the investigated substrate layer system was less than 0.5%, thus the adaptation of both structures allowed to avoid dislocation and stacking faults. It was found that the Nd^{3+} fluorescence and the fluorescence lifetime of the layer were identical with those of the bulk material. Superradiance and waveguiding in a layer of 28 μm thickness were also demonstrated.

Later, Leonyuk et al. [34] reported the LPE growth of NAB epilayers from a $K_2Mo_3O_{10}$-based complex solvent. Spontaneous YAB single crystals without preliminary preparation were used as substrates. The concentration of NAB was 17–20 wt.% and the relative supersaturation σ varied in the range 0.008–0.02. It was shown that the homogeneity of the epitaxial layers depended on the composition, supersaturation, growth temperature and substrate quality (Figure 3).

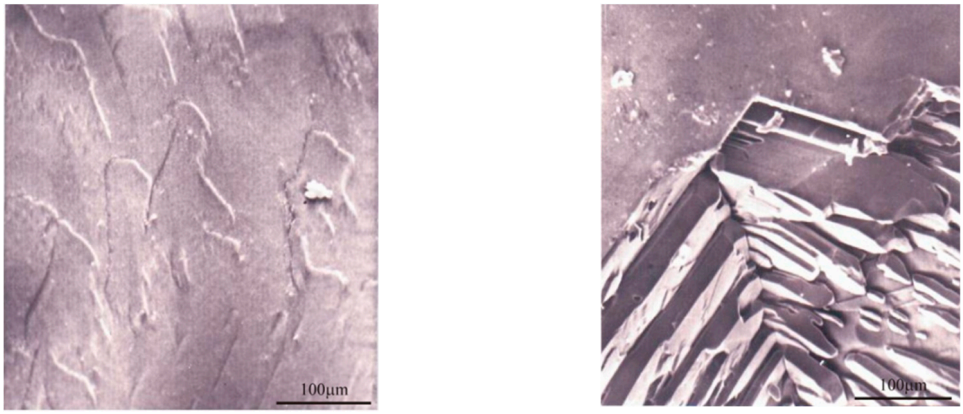

(**a**) (**b**)

Figure 3. $NdAl_3(BO_3)_4$ (NAB) epilayers grown on $YAl_3(BO_3)_4$ (YAB) substrates: (**a**) $\sigma = 0.02$; (**b**) $\sigma = 0.05$ [34].

Newly, NAB epitaxial layers were grown from the system (28 wt.% $NdAl_3(BO_3)_4$–72 wt.%(69.4 wt% $K_2Mo_3O_{10}$–18.1 wt% Nd_2O_3–12.5 wt% B_2O_3) [35]. In these experiments, wafers cut out of monoclinic crystals were used as substrates. As mentioned above, there is still the problem of defining the growth conditions for the NAB polymorphic modifications. According to [23], the low-temperature *R32* modification crystallizes in the narrow temperature range of 870–900 °C during rapid cooling of the system. Under these conditions, it seems almost impossible to obtain large high-quality crystals belonging to the space group *R32*. The expansion of the temperature range within which crystals of an acceptable size can be obtained leads to the formation of samples that are a mixture of two polymorphic modifications: *C2*/*c* (mainly) and *R32*. However, epitaxial layers of rhombohedral phase can be grown within these temperature limits. The structural similarity of polymorphic modifications allows to find comparable planes in both crystals. As a result of crystallographic analysis conducted by Jung et al. [36], it was found that the $\{10\bar{1}1\}$ planes of the hexagonal system (*R32*) are comparable with the $\{11\bar{1}\}$ and {001} planes of the monoclinic one (*C2*/*c*), whereas the hexagonal $\{2\ \bar{1}\ \bar{1}0\}$ and $\{11\ \bar{2}0\}$ prism faces are comparable with the monoclinic {111} and {010} faces. Therefore, in LPE experiments, the $\{11\bar{1}\}$- and {001}-oriented plates cut from the monoclinic NAB bulk crystals (space group *C2*/*c*) were used as substrates for the LPE growth of epitaxial layers. Some NAB films were grown on substrates covered by Pt buffer layers, in order to improve the crystal quality of the epitaxial films. Figure 4 shows typical habit of monoclinic (Figure 4a) and rhombohedral (Figure 4d) NAB crystals, as well as a structural comparison of the substrate and layer planes in the example of the system's (001) wafer/$(10\ \bar{1}1)$ epilayer (Figure 4c and d, respectively).

The thickness of the NAB epilayers was typically 120–260 μm after 24 h of growth depending on the fluxed melt supercooling. The observed linear growth rates of the NAB epilayers were 0.08–0.17 μm/min. The normal growth rate of NAB epilayers on a platinum-covered substrate is lower due to the kinetic barrier relating to the formation of a new layer (Figure 5). XRD investigations have shown that the obtained NAB films are a mixture of two modifications, and the rhombohedron phase prevails.

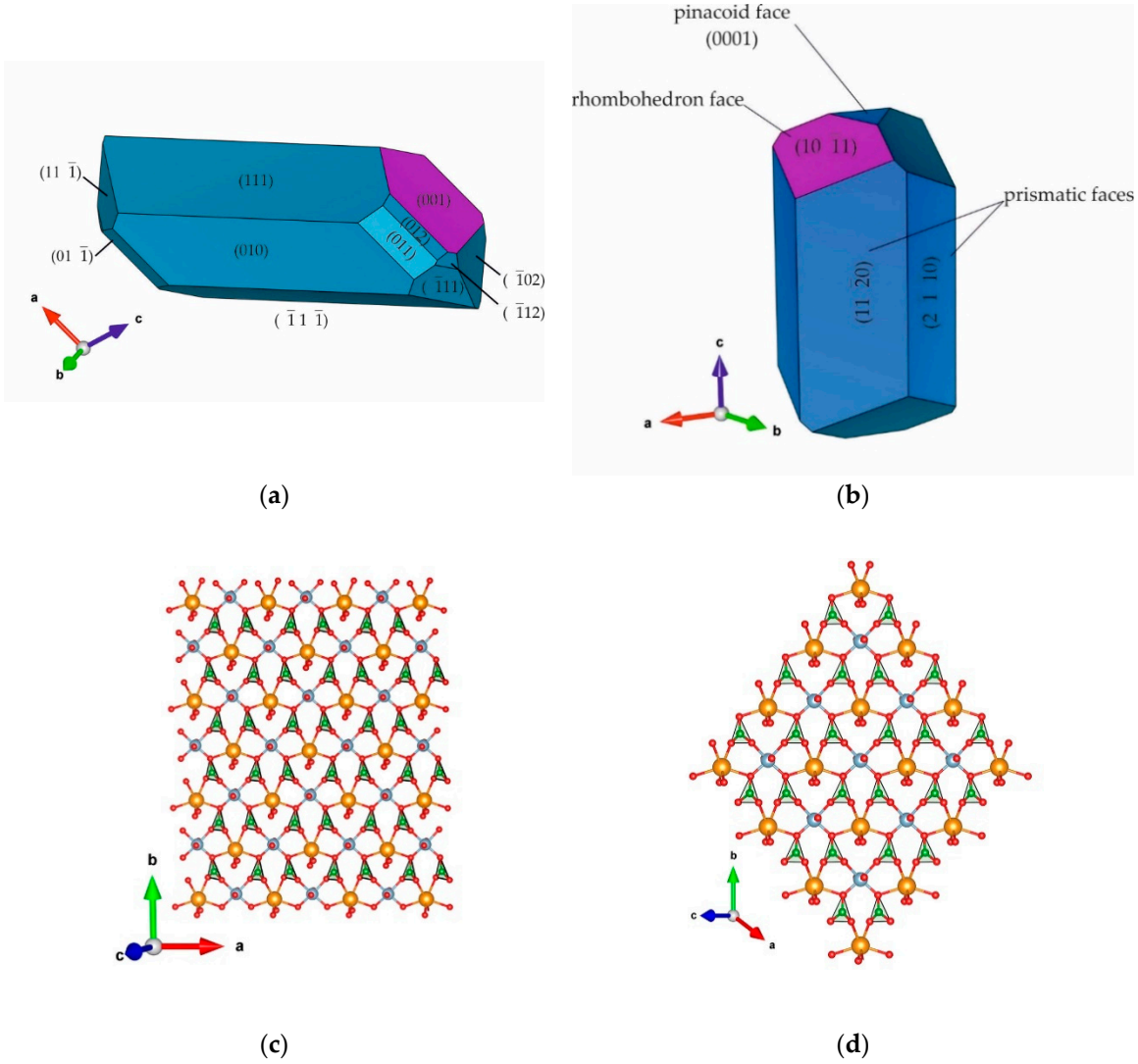

Figure 4. The typical growth habits of NAB monoclinic (**a**) and rhombohedral (**b**) single crystals; NdAl-borates layer perpendicular to the (001) monoclinic plane (**c**) and (10 $\bar{1}$1) rhombohedral plane (**d**) of monoclinic (the green, red, brown and blue balls represent B, O, Nd and Al atoms, respectively). Visualization: VESTA [37].

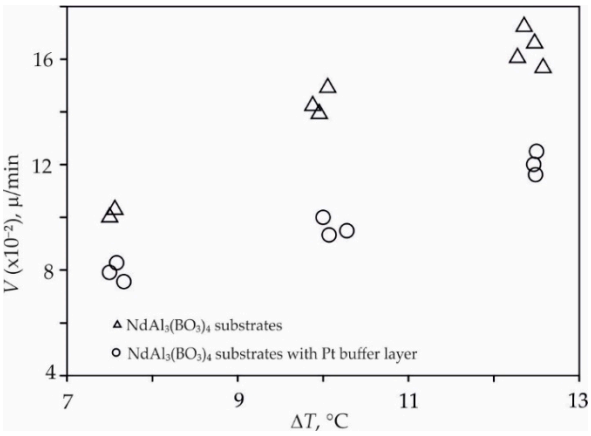

Figure 5. Normal growth rate vs. relative supercooling for NAB epitaxial layers obtained from a 28–71 wt.% (69.4 wt% $K_2Mo_3O_{10}$–18.1 wt% Nd_2O_3–12.5 wt% B_2O_3) solvent [35]. Reprinted from the Journal of Crystal Growth, 401, Volkova E., Maltsev V., Kolganova O., Leonyuk N.I., High-temperature

growth and characterization of (Er,Yb):$YAl_3(BO_3)_4$ and $NdAl_3(BO_3)_4$ epitaxial layers, 547-549, Copyright (2014), with permission from Elsevier.

Comparatively recently, the growth kinetics of YAB epitaxial layers, doped with Er^{3+} and/or Yb^{3+}, were investigated. The lattice parameters of the layers were calculated for different concentrations of Er and/or Yb ions using weighted averages of data from the pure compounds. Known lattice parameters of the stoichiometric solids $YAl_3(BO_3)_4$, $YbAl_3(BO_3)_4$ and $ErAl_3(BO_3)_4$, calculated lattice constants of the grown R-doped YAB epitaxial layers and their related misfit with pure $YAl_3(BO_3)_4$ are listed in Table 1.

Table 1. Lattice parameters of pure YAl-, YbAl- and ErAl-borates, *R*-doped $YAl_3(BO_3)_4$ epitaxial layers and their lattice misfit with YAB at room temperature.

Material	*a*, nm/Misfit with YAB, %	*c*, nm Misfit with YAB, %	Ref.
$YAl_3(BO_3)_4$	0.9289/0.00	0.7239/0.00	[38]
$YbAl_3(BO_3)_4$	0.9251/-0.4	0.7189/-0.6	[39]
$Yb_{0.1}Y_{0.9}Al_3(BO_3)_4$	0.9285/-0.04	0.7234/-0.06	-
$ErAl_3(BO_3)_4$	0.9285/-0.04	0.7222/-0.2	[40]
$Er_{0.04}Y_{0.96}Al_3(BO_3)_4$	0.9288/-0.01	0.7238/-0.01	-
$Er_{0.015}Yb_{0.11}Y_{0.875}Al_3(BO_3)_4$	0.9285/-0.04	0.7233/-0.08	-

Generally, misfit-induced strain in epitaxial layers can be compensated by elastic relaxation or can be relieved via formation of misfit dislocations. The elastic accommodation is possible if the lattice misfit is rather small. Based on extensive data on the LPE-grown garnet layer, Ferrand et al. [28] assumed an elastic relaxation, if f_{latt} is less than 10^{-3}. Further, it seems to be preferable to grow layers with the lattice mismatch slightly negative.

Doping insignificantly effects the thermal expansion coefficients at the T_g. Table 2 shows the thermal expansion coefficients along different crystallographic directions for $YAl_3(BO_3)_4$ and $Er_{0.015}Yb_{0.11}Y_{0.875}Al_3(BO_3)_4$ solids at the growth temperature. The temperature dependence of lattice parameters *a* and *c* for both solids was investigated using the powder diffraction technique in the temperature range of 25–1050 °C [38]. It was demonstrated that, with increasing temperature, the [100] lattice mismatch in the system under consideration increases from 0.02% to 0.04%, whereas the [001] lattice mismatch remains constant at 0.15%. Linear thermal expansion coefficients were evaluated as

$$\alpha = \frac{a_2 - a_1}{a_1(T_2 - T_1)}, \quad (5)$$

where a_2 and a_1 are the values of the parameter at temperatures T_2 and T_1, respectively [41].

Table 2. Linear thermal expansion coefficients of YAB and (Er,Yb):YAB solids [38].

Compound	$\alpha_{[100]}$, 10^{-6} K^{-1}	$\alpha_{[001]}$, 10^{-6} K^{-1}
$YAl_3(BO_3)_4$	4.2	12.97
$Er_{0.015}Yb_{0.11}Y_{0.875}Al_3(BO_3)_4$	4.4	13.17

Since the lattice mismatch between $YAl_3(BO_3)_4$ and $Er_{0.015}Yb_{0.11}Y_{0.875}Al_3(BO_3)_4$ is rather low, the epitaxial growth in the investigated systems can be considered as an almost homoepitaxial process.

Figure 6 shows the scheme of an experimental LPE set-up with vertical loading. The crucible inside the furnace contains the layer constituents dissolved in an appropriate solvent. The substrate is immersed into the supersaturated solution, and the desired layer can be grown. After the growth, the substrate with a layer is slowly withdrawn from the solute.

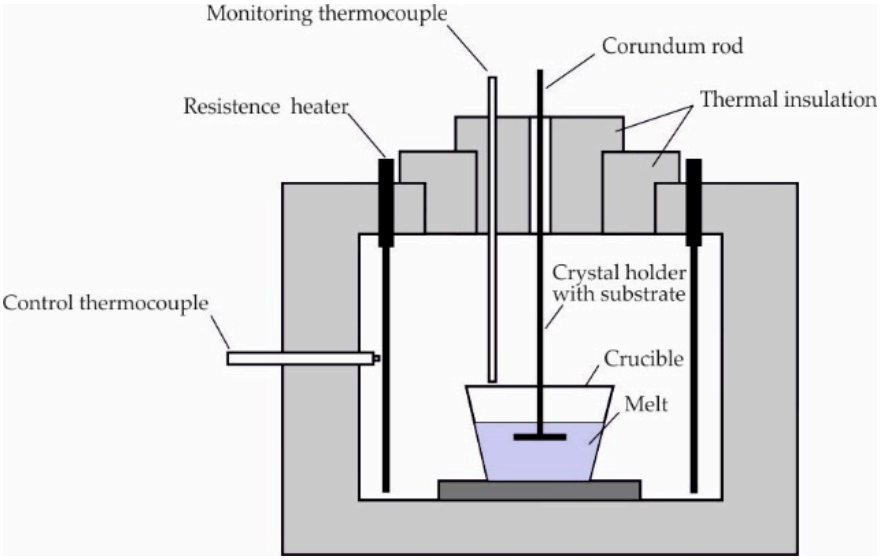

Figure 6. Scheme of the experimental set-up for liquid-phase epitaxy (LPE) [38].

A series of LPE experiments have been carried out to determine the growth kinetics of Er^{3+}- and/or Yb^{3+}-doped $YAl_3(BO_3)_4$ films on the supercooling of high-temperature solutions and growth duration. Epitaxial layers with a 10 at.% ytterbium content were grown on spontaneously obtained YAB crystals without preliminary preparation [42]. The mixture composition corresponded to the YAB/(Er,Yb):YAB concentration of 17 wt% in the 91.0 wt% $K_2Mo_3O_{10}$–8.0 wt% B_2O_3–1.0 wt% Y_2O_3 solvent. The growth rates of the layers were determined to be within the range of 0.07–0.35 μm/min for the interval of fluxed melt supercooling from 5 to 20°C. These data agree well with the result on the kinetics of YAB bulk crystal growth from $K_2Mo_3O_{10}$-based molten solutions [43]. On the whole, the normal growth rate of Yb:YAB films depends linearly on the supercooling of the molten solution (Figure 7). It implies a high level of the growth activation energy due to significant restrictions on the transport of BO_3 groups from the polymerized melt to an isolated state at the solid–liquid phase boundary.

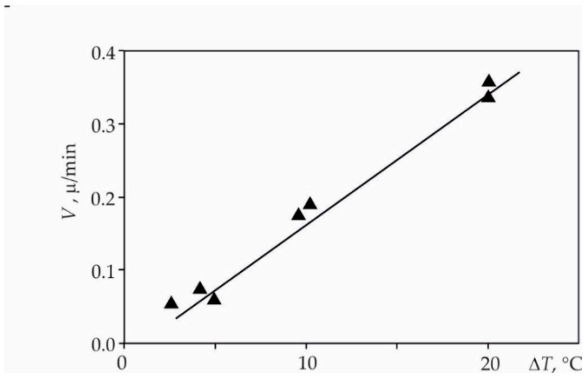

Figure 7. Normal growth rate vs. relative supercooling for Yb(10 at.%):YAB epitaxial layers from a 17–83 wt.% (91.0 wt% $K_2Mo_3O_{10}$–8.0 wt% B_2O_3–1.0 wt% Y_2O_3) solvent [42]. Reprinted from the Journal of Crystal Growth, 275, Volkova E., Leonyuk N.I., Growth of Yb:$YAl_3(BO_3)_4$ thin films by liquid-phase epitaxy, e2467-e2470, Copyright (2005), with permission from Elsevier.

Further LPE experiments have been carried out on plates with different orientation. YAB bulk crystals were cut along the rhombohedral face $\{10\bar{1}1\}$'s faces (Figure 4b). The solvent composition was 88.1.0 wt% $K_2Mo_3O_{10}$–8.6 wt% B_2O_3–3.3 wt% R_2O_3 (where R = Er, Yb) with 17 wt.% of layer-forming constituents in the growth mix [35]. The calculated growth rates of the (Er,Yb):YAB and Er:YAB epitaxial layers were in the range of 0.017–0.31 μm/min (Figure 8). The average Er and Yb

effective distribution coefficient was 0.84 due to minor differences in the size of the Y^{3+}, Er^{3+} and Yb^{3+} cations.

At a relatively low supercooling process ($\Delta T < 7$ °C), the surface morphology of the Er:YAB and (Er,Yb):YAB films was quite good. Surface irregularities were smaller than 50 μm and they could be easily removed from the surface by a polishing procedure (Figure 9a). Based on the data of $Er_{0.015}Yb_{0.11}Y_{0.875}Al_3(BO_3)_4$ growth kinetics, an epitaxial layer of 50 μm thickness for waveguide testing was obtained. Subsequently, the layer surface was polished to laser-grade quality [44]. The optical image of the end face of the Er(1.5 at.%),Yb(11 at.%):$YAl_3(BO_3)_4$ film is shown in Figure 9b. The polished edge looks optically good, the YAB//(Er,Yb):YAB substrate layer interface is sharp and straight without visible defects.

To confirm the crystal nature of the grown layer, its spectroscopic characteristics were investigated. According to Reference [44], the room-temperature absorption and fluorescence spectra were well-correlated with those of bulk (Er,Yb):YAB crystal. The obtained epilayer was tested as a passive optical waveguide. The distribution in the intensity of the outcoupled emission of the Ti:sapphire laser from the end facet of the sample in passive waveguide tests is shown in Figure 10. Multimode passive waveguiding was observed in a 50 μm thick film. Some background light was detected in the substrate, because of ineffective coupling and waveguide losses. The parasitic propagation losses were approximately 2 dB/cm.

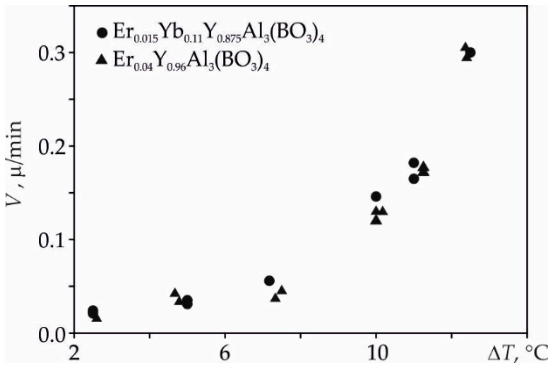

Figure 8. Normal growth rate vs. relative supercooling for Er:YAB and (Er,Yb):YAB epitaxial layers from a 17–83 wt.% (88.1 wt% $K_2Mo_3O_{10}$–8.6 wt% B_2O_3–3.3 wt% Y_2O_3) solvent [35]. Reprinted from the Journal of Crystal Growth, 401, Volkova E., Maltsev V., Kolganova O., Leonyuk N.I., High-temperature growth and characterization of (Er,Yb):$YAl_3(BO_3)_4$ and $NdAl_3(BO_3)_4$ epitaxial layers, 547-549, Copyright (2014), with permission from Elsevier.

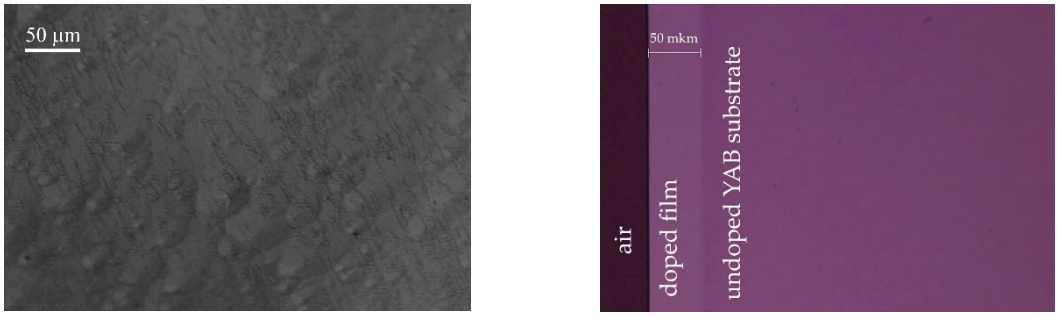

Figure 9. 50 μm thick as-grown (Er,Yb):YAB layer (**a**) and polarized optical image of the polished cross-section of the (Er,Yb):YAB layer on the YAB substrate (**b**).

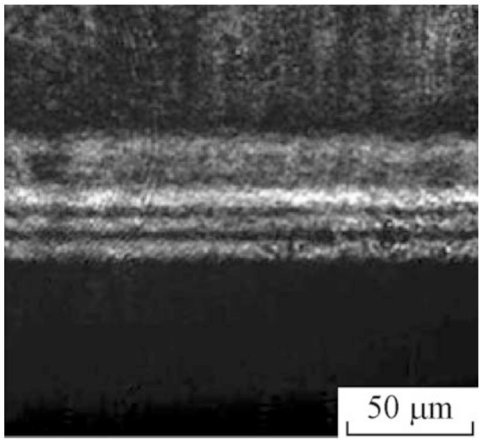

Figure 10. Near-field image of the outcoupled 900 nm light from the (Er,Yb):YAB waveguide [44]. Reprinted from Optical Materials, 32, Tolstik N., Heinrich S., Kahn A., Volkova E., Maltsev V., Kuleshov N., Huber G., Leonyuk N. High-temperature growth and spectroscopic characterization of Er,Yb:$YAl_3(BO_3)_4$ epitaxial thin films, 1377–1379, Copyright (2010), with permission from Elsevier.

Lu and co-workers [45] obtained Nd:YAB epilayers with 9% Nd dopant on an undoped $\{01\bar{1}1\}$ YAB substrate from a $K_2Mo_3O_{10}$-B_2O_3 flux system. The authors estimated the growth kinetics of epitaxial layers (Figure 11). Thus, the growth protocol for LPE of high-quality Nd:YAB films was defined. The LPE conditions were chosen so that the film growth was carried out in the thermodynamic growth mode with no spontaneous nucleation, which occurs for ΔT of 8 °C and more. Nd:YAB thin films were grown at ΔT = 4 °C with a growth rate of about 5 μm/h and exhibited a good surface, high optical quality and homogeneity, and effective waveguiding of the strong luminescence at 1062 nm.

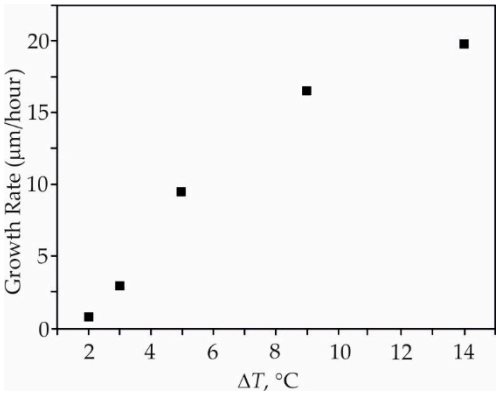

Figure 11. Nd:YAB crystal growth rate on rhombohedral face seed crystal vs. supercooling ΔT [45].

2.2. Polymeric Precursor Method and Sol-Gel Technique

As mentioned above, recent results presented in the literature confirm that ceramic laser materials can be a promising alternative to single crystals because of their simpler manufacturing and lower cost. Transparent RAB-based ceramic composites seem to be very promising because of their potential as a laser medium. Moreover, homogeneous rare-earth borate glassy thin films are promising objects for waveguide structures as there are no grain boundaries, which can lead to high optical losses. A YAB-based glassy borate system is very suitable for this purpose due to the high glass transition temperature (T = 700 °C). Two chemical routes, the sol–gel method and the polymeric precursor method (PP), allow to produce glassy thin films and powders, which can then be used to prepare ceramics. The main differences of these methods are the precursor compounds and the associated chemical reactions [46]. In the case of polymeric precursor synthesis, citric acid and *d*-sorbitol are used as complex formation and polymerization agents, respectively. Carbonates and salts

are commonly used as precursors. The molar ratio of citric acid to elements (metals + boron) was 3:1. The citric acid/d-sorbitol mass ratio was set to 3:2. During the sol–gel process, alkoxides and salts are usually used as precursors and their hydrolysis must be carefully controlled. For layer preparation in the sol–gel process, aluminum acetylacetonate $Al(acac)_3$, tri-i-propylborate $B(OPr^i)_3$, yttrium nitrate hexahydrate $Y(NO_3)_3{\cdot}6H_2O$ and erbium nitrate penta-hydrate $Er(NO_3)_3{\cdot}5H_2O$ as a source for precursor elements dissolved in propionic acid (PropAc) and ethyl alcohol (EtOH) mixtures were used. The sols were prepared in a dry glove box under nitrogen atmosphere, and the partial hydrolysis of the precursors was performed at 80 °C within 1 hour. The molar ratio of (metals+boron):EtOH:PropAc:H_2O was 1:95:55:5. Thin films were obtained by the spin-coating technique on silica glass substrates. After each layer deposition, the films were dried at 80°C for 30 min, and annealed at 400 and 700 °C for 2 h each. This procedure was repeated for each single layer for 7–10 multi-layers. The obtained films were annealed under oxygen at 740 and 780 °C during 2 h for the PP and SG methods, respectively. Thus, this approach resulted in the synthesis of amorphous (glassy) layers with a high-quality surface, that are fundamental for low loss waveguides [46,47]. The authors of Reference [46] stated that dense and chemically homogeneous thin films without grain boundaries can be obtained due to the glass transition of the matrix.

Maia et al. [47] reported on $Er_{0.1}Y_{0.9}Al_3(BO_3)_4$ nanometer-size powders and amorphous thin films obtained by the SG method using a new route. During the experiments, propionic acid was found to act as a good chelating agent for Y^{3+} and Er^{3+} ions. The resulting sols were very stable and allowed homogeneous gels and transparent amorphous thin films to be produced. Furthermore, the propionic acid prevents the sol precipitation. The solution stability and thin film monolayer thickness were estimated depending on the solvent evaporation at the different molar solvent quantities. As a result, a new route and solvents combination were used for the first time to prepare stable and transparent sols and then homogeneous gels of Er:YAB compounds. Stable $Er_{0.1}Y_{0.9}Al_3(BO_3)_4$ amorphous powders with glass transition at 746 °C and a crystallization temperature around 830 °C were obtained. Further annealing of amorphous powders at 1150 °C allowed to prepare crystalline nanometer-sized powder samples. Dense and homogeneous glassy thin films, without cracks, porouses, organic groups and boron losses were obtained after annealing in the temperature range of 746–830 °C.

As reported in Reference [48], further optimization of $Er_{0.1}Y_{0.9}Al_3(BO_3)_4$ thin films for integrated optics has been carried out. Films were obtained on silica and silicon (111) wafers by the spin-coating technique from solutions previously prepared by the PP method. Epitaxial structures of 400–800 nm thick have been obtained using the multi-layer process and following annealing at different temperatures. It was found that a 10-multi-layer process allows to obtain thin films around 775 nm thick at the optimized heat treatment temperature of 740 °C. Deposited films were amorphous until 740 °C. The increase in annealing temperature led to the crystallization process at 780 °C after 2 h of annealing with the formation of the $Al_4B_2O_9$ phase. Thin films annealed at 740 °C demonstrated better densification associated with the higher refractive index of ~1.64 at 980 nm and good waveguiding characteristics with high light-coupling efficiency (~70%) close to the theoretical limit (80%). The crystallization process starting above 780 °C strongly damaged the optical and waveguiding properties due to grain and void formation.

A planar waveguide structure based on $Er_xY_{1-x}Al_3(BO_3)_4$ (x = 0.02, 0.05, 0.1, 0.3 and 0.5) multi-layer thin films was obtained by the PP and SG methods using spin-coating by the authors [46]. The deposition was carried out on silica glass substrates and involved a multi-layer process (7–10 layers). The obtained films prepared using the polymeric precursor technique were annealed in an oxygen atmosphere at 740 °C, while using the sol–gel method, at 780 °C. Optical transmission, photoluminescence emission, lifetime and waveguiding properties of Er:YAB planar waveguides were investigated. The propagation losses of the planar waveguides measured at 632.8 and 1550 nm varied from 0.63 to 0.88 dB/cm. The photoluminescence spectra and radiative lifetimes of the $Er^{3+}\,{}^4I_{13/2}$ energy level were measured in waveguiding geometry. The photoluminescence decay was found to be single exponential with lifetimes between 640 and 200 μs, depending on the erbium concentration and synthesis method.

Subsequently, the structural, microstructural and optical properties of $Er_xY_{1-x}Al_3(BO_3)_4$ multi-layer thin films with x = 0.02, 0.05, 0.1, 0.3 and 0.5 prepared by means of the PP and SG chemical routes were optimized to obtain the best waveguiding properties [49,50]. Films obtained using the polymeric precursor route, especially for the compositions with x = 0.10, demonstrated the lowest propagation loss value (0.52 ± 0.14 dB/cm at k = 633 nm) and was found to be the most promising for waveguiding.

3. RAB Related Glass-Ceramics Materials

The significant content of boron oxide in the $RAl_3(BO_3)_4$-solvent systems provides a high glass-forming ability of the melt and possibility of fabrication of transparent glasses and glass–ceramic samples with a composition identical to that of crystals. There are a number of reports on the synthesis and characterization of YAB-based glasses. Thus, $Sm_xY_{1-x}Al_3(BO_3)_4$ crystalline powders and glasses with the chemical composition 2.5 mol.% $(Sm_xY_{1-x})_2O_3$–37.5 mol.% Al_2O_3–50 mol% B_2O_3 (x = 0.004–1) were synthesized by the solid-phase reactions technique and, respectively, by melting of the corresponding oxides [51]. It was shown that for this composition, the transition from polycrystals to glasses occurred at a relatively high temperature ~1470 °C. XRD analysis confirmed the huntite-like structure of the polycrystals, whereas glasses were completely amorphous, with no detectable contribution from the crystalline phases. A comparative analysis of the spectral and kinetic properties of the Sm^{3+} ions luminescence in Sm:YAB polycrystals and glasses with identical composition was carried out. A comparison of the excitation spectra of the luminescence and decay kinetics of the polycrystals and glasses indicated a decrease in covalence of the Sm-O bond. It was shown that the amorphous matrix exhibited randomly distributed units having common features with the huntite-type structure and were virtually free from R-O-R bonds. Thus, the cation ensemble structure is preserved, and an extension of the Sm-Sm distance from 0.59 to 0.67 nm in glass is observed. Meanwhile, some BO_3 polyhedra transform into BO_4 groups. This led to an increase in the quantum yield of luminescence, making these glasses perfect host matrices for heavily *R*-doped optical materials [52].

Ziyatdinova et al. calculated the Judd–Ofelt parameters for glasses with the following compositions (in molar fraction): 1.0 Ce_2O_3–6.0 Tb_2O_3–3.0 Y_2O_3–30.0 Al_2O_3–60.0 B_2O_3 and 6.0 Tb_2O_3–4.0 Y_2O_3–30.0 Al_2O_3–60.0 B_2O_3 [53]. The glasses were synthesized at 1480 °C, quenched on a metal plate, pressed to a thickness of about 1.5–2 mm and then annealed at a temperature close to the growth one. Several glass properties like density, refractive indices and terbium concentration in 1 cm^3 of glass were investigated. It was found that Tb–O–Ce bonds are practically absent in glassy samples, i.e., the rare-earth polyhedra do not share common vertices despite the disordered structure of the matrix. Malashkevich et al. recently reported results on synthesized Yb^{3+}-doped YAB glasses by the conventional melt-quenching technique [54]. The spectral-luminescence characteristics of prepared glasses were investigated. Yb:YAB glasses demonstrated excellent thermal stability, as heat treatment at 720 °C did not affect the spectra of the matrix. They also showed a high threshold of the laser-induced destruction of such glasses' surfaces (27 ± 3 J/cm^2 and nonlinear refraction index close to 2.2 × 10^{-13} esu). The Yb^{3+} ions in these glasses form one type of optical center with the radiation decay constant at 870 ± 40 μs. Yb-doped glasses exhibit low efficiencies of cooperative luminescence for Yb -Yb pairs. The lasing was obtained on a 2.1 mm thick glass plate with a threshold of 60 W/mm^2 estimated by the specific absorbed power.

The authors [55,56] synthesized GC materials based on YAl- and GdAl-borates in a wide temperature range. Opaque GC samples (glazes) were synthesized, when the starting mixture composition corresponded to the borate stoichiometry. Transparent materials were obtained at the excess of boron anhydride in the initial mixture of 100 wt.% (Figure 12). It was found that the optimal temperature for the synthesis of GC materials based on *R*AB corresponds to 1250 and 1350 °C for Y- and Gd-borates, respectively.

(**a**) (**b**) (**c**)

Figure 12. As-obtained ceramics: (**a**) transparent YAB-based glass–ceramic composites; (**b**) GdAB-containing glaze; (**c**) transparent GdAB-based glass–ceramic composites [56]. Figures 12a and 12b reprinted from the Journal of Crystal Growth, 457, Naprasnikov D.A., Maltsev V.V., Leonyuk N.I., Gorbachenya K.N., Kurilchik S.V., Kisel V.E., Kuleshov N.V. Micro-crystallization and spectroscopic properties of Er, Yb:RAl-borates (R = Y, Gd) obtained in $RAl_3(BO_3)_4$–$K_2Mo_3O_{10}$–B_2O_3–R_2O_3 and $RAl_3(BO_3)_4$–B_2O_3 systems, 302–306, Copyright (2017), with permission from Elsevier.

Transparent YAB glass samples were completely amorphous with no detectable contribution from the crystalline phases. X-ray diffraction patterns of these samples indicated no detectable peaks, proving the amorphous structure. Scanning electron microscope (SEM) images of the quenched YAB-based glasses showed no possible microcrystals within the limits of the SEM resolution (Figure 13a). On the contrary, XRD patterns of the opaque YAB GC composites show the presence of the YAl-borate crystalline phase. SEM images of the YAB glazes clearly show cavities (Figure 13b). The authors attribute their origin to the removal of volatile components in the process of crystallization. Microprobe analysis showed that the glass matrix has areas with different composition, which may also indicate the formation of the nanoscale crystalline phase in these composites.

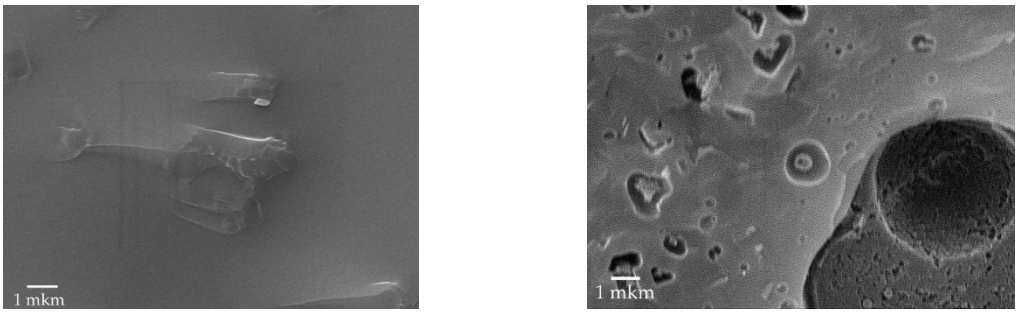

(**a**) (**b**)

Figure 13. SEM images of transparent (**a**) and opaque (**b**) YAB-based glass–ceramics.

Transparent GdAB-based composites exhibit needle-like microcrystals (Figure 14a), while in GdAB-based glazes, two types of crystalline phases several micrometers in size were observed: elongated needle-like microcrystals with a length/width ratio of ~ 10/1 and small idiomorphic prismatic individuals (Figure 14b) [56].

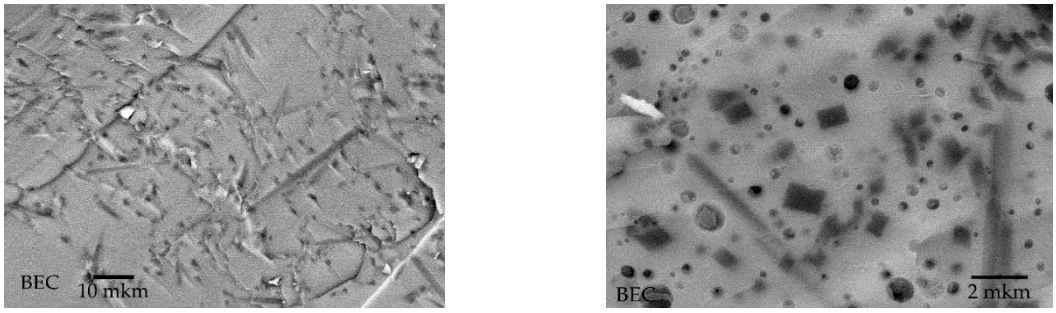

(**a**) (**b**)

Figure 14. Backscattering SEM images of (**a**) transparent and (**b**) opaque GdAB-based glass–ceramics [56]. Figure 14b reprinted from the Journal of Crystal Growth, 457, Naprasnikov D.A., Maltsev V.V., Leonyuk N.I., Gorbachenya K.N., Kurilchik S.V., Kisel V.E., Kuleshov N.V. Micro-crystallization and spectroscopic properties of Er, Yb:RAl-borates (R = Y, Gd) obtained in $RAl_3(BO_3)_4$–$K_2Mo_3O_{10}$–B_2O_3–R_2O_3 and $RAl_3(BO_3)_4$–B_2O_3 systems, 302–306, Copyright (2017), with permission from Elsevier.

XRD investigations confirm the presence of the crystalline phase in the as-obtained GdAB-based composites [55,56]. The positions of the detected peaks are in good agreement with the reference data. In the case of the GdAB GC glaze, two crystalline phases were identified: GdAB and Al_5BO_9.

The distribution of chemical elements in the GdAB-based composite was analyzed. Different concentration profiles for the elements within the selected sample section were identified. The distribution of gadolinium is uniform, while oxygen and aluminum are concentrated in areas where crystalline fractions were detected in the glass matrix (Figure 15). The volumetric X-ray tomography was used to obtain a series of three-axis planar images for the GdAB-based composite (Figure 16). Two phases are clearly detectable in the images: dark, corresponding to microcrystals with a lower X-ray absorption, and light, corresponding to the glass matrix, and characterized by high absorption. Further, several cavities were observed. The volumetric rendering of the GdAB-based composite of a 1 × 1 × 1 mm^3 size clearly demonstrates the spatial distribution of the crystal phase in it. Herewith, the crystalline phase content is up to 32.5%, while the content of cavities corresponds to 0.35% [56].

The structural studies of transparent YAB-based GC samples using IR spectroscopy demonstrate absorption bands of stretching vibrations at 1380 and 1240 cm^{-1} and deformation vibrations in the range ~700 cm^{-1} assigned to the BO_3 triangles, as well as weaker bands of stretching vibrations at ~1090, 1030 cm^{-1}, which indicates the presence of BO_4 groups. The IR spectra of the stoichiometric glazes exhibit a large number of absorption bands in the range 1270–1390 cm^{-1} and 880–920 cm^{-1} attributed to stretching vibrations of BO_3 and BO_4 groups, respectively. Further, absorption bands are observed at 700 cm^{-1} at lower frequencies. Thus, the formation of new bonds between BO_3 triangles and BO_4 tetrahedra through the common oxygen atoms can be assumed.

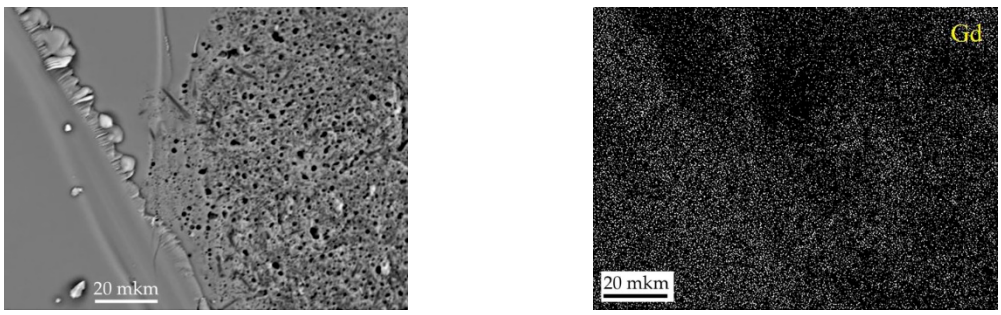

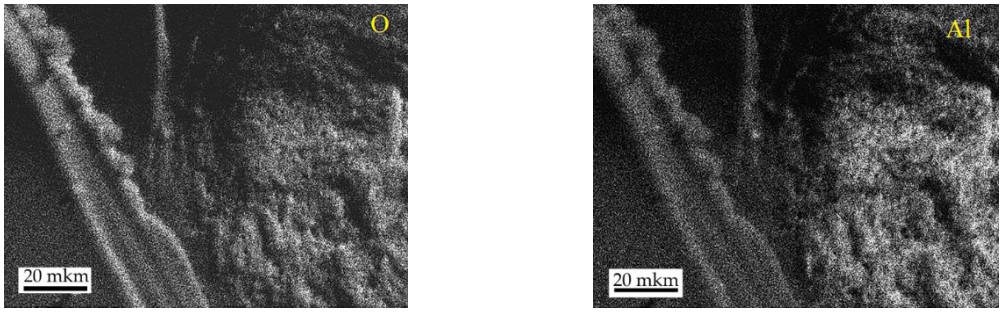

Figure 15. The distribution of chemical elements in the GdAB-based composite.

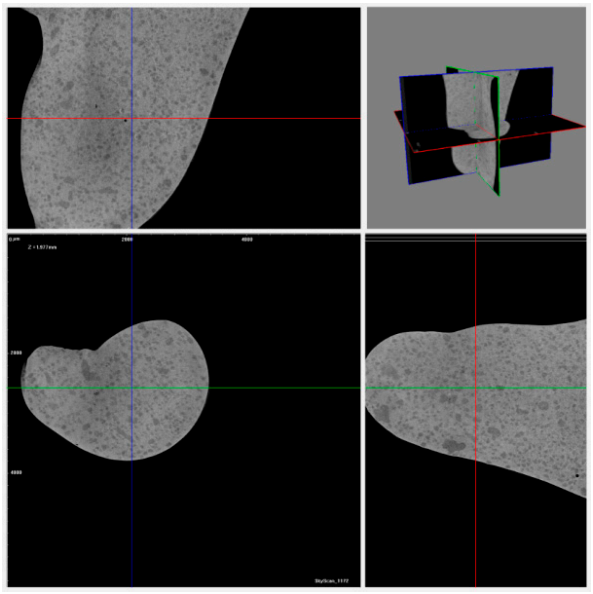

Figure 16. Three-axes slice for the GdAB-based composite.

The IR spectra of the transparent and opaque GdAB-containing composites show absorption bands of isolated BO_3 groups in the range 1260–1375 cm^{-1} and 670–830 cm^{-1} attributed to stretching and deformation vibrations, respectively. Moreover, vibrations of the Al^{3+} cation in octahedral oxygen coordination at 570–460 cm^{-1} are observed. Weak bands at 1200–900 cm^{-1} assigned to the BO_4 groups' vibrations were indicated. The analysis of the IR spectra for the YAB- and GdAB-based composites indicates the presence of the crystalline phase in the glass matrix [6].

Further, absorption and luminescence spectra were measured for the YAB- and GdAB-based GC composites, doped with Er^{3+} and/or Yb^{3+} at 850–1050 nm and around 1500 nm. It was shown that the absorption spectrum of the glass–ceramic composite based on (Er,Yb):YAB at 850–1050 nm shows an absorption band with a width of about 85 nm at 900–1000 nm with a high peak at 975 nm, where the absorption coefficient reaches 9.1 cm^{-1}. This absorption band is composed of overlapped bands produced by both erbium $^4I_{15/2} \rightarrow {}^4I_{11/2}$ and ytterbium $^2F_{7/2}$–$^2F_{5/2}$ transitions. It was shown that the absorption spectra of the YAB GC composites co-activated with Er and Yb are comparable with the spectra of the Yb-doped phosphate glasses [6,56]. The spectrum at a wavelength of about 1500 nm was attributed to the $^4I_{15/2}$-$^4I_{13/2}$ energy level transition of the Er^{3+} ions. There is a broad absorption band with full width at a half maximum of 73 nm with a peak of 0.25 cm^{-1} at 1525 nm. The decay curve demonstrates an exponential decay with a time constant of 440 μs, and it defines the $^4I_{13/2}$ energy level lifetime of the erbium cations. The lifetime of the Yb^{3+} cation in the Yb-doped glass–ceramic composite was 780 ± 10 μs, while in the (Er,Yb)-activated samples, this value was reduced to 190±10

μs. The energy transfer efficiency was found to be as high as 75.6%. Similar spectroscopic characteristics were obtained for the (Er,Yb):GdAB glass–ceramic materials.

Lorenzi et al. [57] investigated the radio- and photoluminescence properties of *R*-doped YAB glasses with a general composition of 10.0 ($Ce_xTb_yY_{(1-x-y)}$)–30.0 Al_2O_3–60.0 B_2O_3. Ce-doped glasses exhibit optical features ascribable to preferential location of rare-earth ions in sites with specific geometry similar to that observed in crystalline structures. It was shown that that Ce emission was not compromised even at high doping levels of 9% mol. At a low doping level, the Ce^{3+} cations are preferably formed by trigonal prism polyhedra, as occurs in crystalline materials with a huntite-type structure with similar composition. Ce ions can be used as an activator to enhance Tb^{3+} luminescence. According to the results obtained, the investigated glassy system demonstrates radio- and photoluminescence emission efficiencies and performances similar to those of crystalline solids.

4. Conclusions

An analysis of the existing literature data indicates that *R*AB epitaxial layers, glasses and glass–ceramic composites are rather promising materials with several additional advantages that extend the field of application of huntite-type borate materials. Crystalline epitaxial layers of RAl-borates can be obtained using the LPE technique, as these compounds melt incongruently. Alternatively, polymeric precursor and sol–gel methods are used to produce amorphous films. In both cases, *R*AB compounds are considered to be perspective hosts which exhibit potential waveguide developments. Few studies on the synthesis and characterization of RAB glass systems show their perspective as a matrix for highly doped active media with low concentration quenching of luminescence, making this family of glasses a rather promising candidate for scintillating and photonic applications. LPE growth, as well as the polymeric precursor and sol–gel methods, are well-developed, proven techniques for obtaining complex oxide compounds. For huntite-type materials, the main problem concerns the development of fabricating technology in order to obtain high-quality samples. These investigations represent a new and interesting challenge towards the realization of a material poorly studied before. So far, only a few groups have conducted research on the synthesis and characterization of huntite-type borate thin films and glass–ceramics materials. Nevertheless, the large potential of gain in RAB thin films and glass–ceramic composites may become more visible within the next decade.

Author Contributions: E.A.V., D.A.N. and N.I.L. contributed to this overview. All authors have read and agreed to the published version of the manuscript.

Funding: This research on LPE was funded by Russian Science Foundation, grant number 19-12-00235, investigations on GC were supported in part by the RFBR grant number 18-29-12091mk

Conflicts of Interest: The authors declare no conflicts of interest.

References

1. Ballman, A.A. A new series of synthetic borates isostructural with the carbonate mineral huntite. *Am. Mineral.* **1962**, *47*, 1380–1383.
2. Mills, A.D. Crystallographic Data for New Rare Earth Borate Compounds, $RX_3(BO_3)_4$. *Inorg. Chem.* **1962**, *1*, 960–961, doi:10.1021/ic50004a063.
3. Hong, H.-P.; Dwight, K. Crystal structure and fluorescence lifetime of $NdAl_3(BO_3)_4$, a promising laser material. *Mater. Res. Bull.* **1974**, *9*, 1661–1665, doi:10.1016/0025-5408(74)90158-5.
4. Jarchow, O.; Lutz, F.; Klaska, K.H. Polimorphie und fehlordnung von $NdAl_3(BO_3)_4$. *Z. Kristallogr.* **1979**, *149*, 162–164.
5. Wang, G.; He, M.; Luo, Z. Structure of β-NdAl3(BO3)4 (NAB) crystals. *Mat. Res. Bull.* **1991**, *26*, 1085–1089.
6. Leonyuk, N.I.; Maltsev, V.V.; Volkova, E.A.; Koporulina, E.V.; Kuleshov, N.V.; Kisel, V.E.; Gorbachenya, K.N. Ytterbium and Erbium Co-doped Rare-Earth Aluminum Borate Crystals as New Materials for Eye-Safe Lasers: Flux Growth and Characterization. In *Handbook of Ecomaterials*; Springer Science and Business Media LLC: Berlin/Heidelberg, Germany, 2018; pp. 1–46.

7. Kuz'Micheva, G.M.; Kaurova, I.; Rybakov, V.B.; Podbel'Skiy, V.V. Crystallochemical Design of Huntite-Family Compounds. *Crystals* **2019**, *9*, 100, doi:10.3390/cryst9020100.
8. Leonyuk, N. Recent developments in the growth of $RM_3(BO_3)_4$ crystals for science and modern applications. *Prog. Cryst. Growth Charact. Mater.* **1995**, *31*, 279–312, doi:10.1016/0960-8974(96)83731-4.
9. Aka, G.; Viegas, N.; Teisseire, B.; Godard, J. Flux growth and characterization of rare-earth-doped non-linear huntite-type borate crystals: $Y_{1-x}Nd_x(Al_{0.7}Ga_{0.3})_3(BO_3)_4$ and $Y_{1-x}Yb_xAl_3(BO_3)_4$. *J. Mater. Chem.* **1995**, *5*, 583–587, doi:10.1039/jm9950500583.
10. Koporulina, E.; Leonyuk, N.; Hansen, D.; Bray, K. Flux growth and luminescence of Ho:$YAl_3(BO_3)_4$ and $PrAl_3(BO_3)_4$ crystals. *J. Cryst. Growth* **1998**, *191*, 767–773, doi:10.1016/s0022-0248(98)00347-9.
11. Jaque, D.; Capmany, J.; Solé, J.G. Red, green, and blue laser light from a single Nd:$YAl_3(BO_{34}$crystal based on laser oscillation at 1.3 μm. *Appl. Phys. Lett.* **1999**, *75*, 325–327, doi:10.1063/1.124364.
12. Dekker, P.; Dawes, J.; Piper, J.A.; Liu, Y.; Wang, J. 1.1 W CW self-frequency-doubled diode-pumped Yb:$YAl_3(BO_3)_4$ laser. *Opt. Commun.* **2001**, *195*, 431–436, doi:10.1016/s0030-4018(01)01347-5.
13. Dominiak-Dzik, G.; Ryba-Romanowski, W.; Kovacs, L.; Beregi, E. Effect of temperature on luminescence and VUV to visible conversion in the $YAl_3(BO_3)_4:Dy^{3+}$ (YAB:Dy) crystal. *Radiat. Meas.* **2004**, *38*, 557–561, doi:10.1016/j.radmeas.2004.03.015.
14. Li, J.; Wang, J.; Cheng, X.; Hu, X.; Wang, X.; Zhao, S. Growth, optical properties and defects of Tb:$YAl_3(BO_3)_4$ crystal. *Mater. Lett.* **2004**, *58*, 1096–1099, doi:10.1016/j.matlet.2003.08.026.
15. Chen, Y.J.; Lin, Y.F.; Gong, X.H.; Tan, Q.G.; Luo, Z.D.; Huang, Y.D. 2.0 W diode-pumped Er:Yb:$YAl_3(BO_3)_4$ laser at 1.5–1.6 μm. *Appl. Phys. Lett.* **2006**, *89*, 241111, doi:10.1063/1.2404969.
16. Tolstik, N.A.; Kurilchik, S.V.; Kisel, V.E.; Kuleshov, N.; Maltsev, V.V.; Pilipenko, O.V.; Koporulina, E.; Leonyuk, N.I. Efficient 1 W continuous-wave diode-pumped Er,Yb:$YAl_3(BO_3)_4$ laser. *Opt. Lett.* **2007**, *32*, 3233–3235, doi:10.1364/ol.32.003233.
17. Lagatsky, A.; Kisel, V.E.; E Troshin, A.; A Tolstik, N.; Kuleshov, N.; I Leonyuk, N.; E Zhukov, A.; Rafailov, E.U.; Sibbett, W. Diode-pumped passively mode-locked Er,Yb:$YAl_3(BO_3)_4$ laser at 1.5–1.6 microm. *Opt. Lett.* **2008**, *33*, 83–85.
18. Tolstik, N.A.; Kisel, V.E.; Kuleshov, N.V.; Maltsev, V.V.; Leonyuk, N.I. Er,Yb:$YAl_3(BO_3)_4$—Efficient 1.5 mkm laser crystal. *Appl. Phys.* **2009**, *97*, 357–362.
19. Jaque, D.; Enguita, O.; Caldino, U.C.; RamírezM.O.; SoléJ.G.; Zaldo, C.; Santiuste, J.M.; Jiang, A.D.; Luo, Z.D. Optical characterization and laser gain modeling of a $NdAl_3(BO_3)_4$ (NAB) microchip laser crystal. *J. Appl. Phys.* **2001**, *90*, 561–569, doi:10.1063/1.1379777.
20. Xue, D.; Zhang, S. Calculation of the nonlinear optical coefficient of the crystal. *J. Phys. Condens. Matter* **1996**, *8*, 1949–1956, doi:10.1088/0953-8984/8/12/009.
21. Jaque, D.; Enguita, O.; SoléJ.G.; Jiang, A.D.; Luo, Z.D. Infrared continuous-wave laser gain in neodymium aluminum borate: A promising candidate for microchip diode-pumped solid state lasers. *Appl. Phys. Lett.* **2000**, *76*, 2176–2178, doi:10.1063/1.126289.
22. Lutz, F.; Huber, G. Phosphate and borate crystals for high optical gain. *J. Cryst. Growth* **1981**, *52*, 646–649, doi:10.1016/0022-0248(81)90355-9.
23. Kumar, J.; Thirumavalavan, M.; Gnanam, F.; Ramasamy, P.; Bocelli, G. Growth, morphological and structural investigations of neodymium aluminium borate crystals from different flux systems. *J. Cryst. Growth* **1990**, *100*, 651–654, doi:10.1016/0022-0248(90)90266-n.
24. Deubener, J.; Allix, M.; Davis, M.; Durán, A.; Höche, T.; Honma, T.; Komatsu, T.; Krüger, S.; Mitra, I.; Müller, R.; et al. Updated definition of glass-ceramics. *J. Non-Crystall. Solids* **2018**, *501*, 3–10, doi:10.1016/j.jnoncrysol.2018.01.033.
25. Scheel, H.J. *Introduction to Liquid Phase Epitaxy*; Wiley: Hoboken, NJ, USA, 2007; pp. 1–19.
26. Nelson, H. Epitaxial growth from the liquid state and its application to the fabrication of tunnel and laser diodes. *RCA Rev.* **1963**, *24*, 603.
27. Linares, R.C. Epitaxial growth of narrow linewidthyttrium iron garnet films. *J. Cryst. Growth* **1968**, *3*, 443–446, doi:10.1016/0022-0248(68)90196-6.
28. Ferrand, B.; Chambaz, B.; Couchaud, M. Liquid phase epitaxy: A versatile technique for the development of miniature optical components in single crystal dielectric media. *Opt. Mater.* **1999**, *11*, 101–114, doi:10.1016/s0925-3467(98)00037-8.
29. Vegard, L. Die constitution der mischkristalle und die raumfüllung der atome. *Z. Phys.* **1921**, *5*, 17–26. https://doi.org/10.1007/BF01349680.

30. Lutz, F.; Leiss, M.; Müller, J. Epitaxy of $NdAl_3(BO_3)_4$ for thin film miniature lasers. *J. Cryst. Growth* **1979**, *47*, 130–132, doi:10.1016/0022-0248(79)90169-6.
31. Lutz, F.; Rüppel, D.; Leiss, M. Epitaxial layers of the laser material $Nd(Ga, Cr)_3(BO_3)_4$. *J. Cryst. Growth* **1980**, *48*, 41–44, doi:10.1016/0022-0248(80)90191-8.
32. Ghez, R.; Giess, E. Liquid phase epitaxial growth kinetics of magnetic garnet films grown by isothermal dipping with axial rotation. *Mater. Res. Bull.* **1973**, *8*, 31–42, doi:10.1016/0025-5408(73)90091-3.
33. Ghez, R.; Giess, E. The temperature dependence of garnet liquid phase epitaxial growth kinetics. *J. Cryst. Growth* **1974**, *27*, 221–226, doi:10.1016/s0022-0248(74)80067-9.
34. Leonyuk, N.; Leonyuk, L. Growth and characterization of $RM_3(BO_3)_4$ crystals. *Prog. Cryst. Growth Charact. Mater.* **1995**, *31*, 179–278, doi:10.1016/0960-8974(96)83730-2.
35. Volkova, E.; Maltsev, V.; Kolganova, O.; Leonyuk, N. High-temperature growth and characterization of (Er,Yb):$YAl_3(BO_3)_4$ and $NdAl_3(BO_3)_4$ epitaxial layers. *J. Cryst. Growth* **2014**, *401*, 547–549, doi:10.1016/j.jcrysgro.2014.01.035.
36. Jung, S.-T.; Kang, J.-K.; Chung, S.-J. Crystal growth and X-ray topography of $NdAl_3(BO_3)_4$. *J. Cryst. Growth* **1995**, *149*, 207–214, doi:10.1016/0022-0248(94)00972-4.
37. Momma, K.; Izumi, F. VESTA 3for three-dimensional visualization of crystal, volumetric and morphology data. *J. Appl. Crystallogr.* **2011**, *44*, 1272–1276, doi:10.1107/s0021889811038970.
38. Volkova, E.; Ksenofontov, D.A.; Maltsev, V.V.; Leonyuk, N.I.; Kabalov, Y.K.; Barilo, S.N.; Bychkov, G.L.; Tolstik, N.A.; Kuleshov, N. Liquid-phase epitaxy of single-crystal erbium-ytterbium codoped $YAl_3(BO_3)_4$ layers as key components of planar waveguides. *Inorg. Mater.* **2011**, *47*, 979–982, doi:10.1134/s002016851109024x.
39. Xu, Y.; Gong, X.; Chen, Y.; Huang, M.; Luo, Z.; Huang, Y. Crystal growth and optical properties of $YbAl_3(BO_3)_4$: A promising stoichiometric laser crystal. *J. Cryst. Growth* **2003**, *252*, 241–245, doi:10.1016/s0022-0248(03)00863-7.
40. Malakhovskii, A.; Kutsak, T.; Sukhachev, A.; Aleksandrovsky, A.S.; Krylov, A.S.; Gudim, I.; Molokeev, M.S. Spectroscopic properties of $ErAl_3(BO_3)_4$ single crystal. *Chem. Phys.* **2014**, *428*, 137–143, doi:10.1016/j.chemphys.2013.11.008.
41. Filatov, S.K. Vysokotemperaturnaya Kristallografiya (HighTemperature Crystallography); Springer: Leningrad, Russia, 1990.
42. Volkova, E.; Leonyuk, N. Growth of Yb:$YAl_3(BO_3)_4$ thin films by liquid-phase epitaxy. *J. Cryst. Growth* **2005**, *275*, e2467–e2470, doi:10.1016/j.jcrysgro.2004.11.378.
43. Azizov, A.V.; Leonyuk N.I. The effect of supersaturation and temperature on the rate of growth of $YAl_3(BO_3)_4$ crystals from molten solution. *J. Cryst. Growth* **1981**, *54*, 296–298, doi:10.1016/0022-0248(81)90473-5.
44. Tolstik, N.A.; Heinrich, S.; Kahn, A.; Volkova, E.; Maltsev, V.; Kuleshov, N.; Huber, G.; Leonyuk, N. High-temperature growth and spectroscopic characterization of Er,Yb:$YAl_3(BO_3)_4$ epitaxial thin layers. *Opt. Mater.* **2010**, *32*, 1377–1379, doi:10.1016/j.optmat.2010.03.016.
45. Lu, Y.; Dekker, P.; Dawes, J. Liquid-Phase Epitaxial Growth and Characterization of Nd:$YAl_3(BO_3)_4$ Optical Waveguides. *Crystals* **2019**, *9*, 79, doi:10.3390/cryst9020079.
46. Maia, L.; Mastelaro, V.R.; Hernandes, A.; Fick, J.; Ibáñez, A. Er:$YAl_3(BO_3)_4$ glassy thin films from polymeric precursor and sol-gel methods: Waveguides for integrated optics. *Thin Solid Films* **2009**, *517*, 6584–6587, doi:10.1016/j.tsf.2009.04.040.
47. Maia, L.; Mastelaro, V.R.; Pairis, S.; Hernandes, A.C.; Ibanez, A. A sol–gel route for the development of rare-earth aluminum borate nanopowders and transparent thin films. *J. Solid State Chem.* **2007**, *180*, 611–618, doi:10.1016/j.jssc.2006.11.016.
48. Maia, L.; Ibanez, A.; Fick, J.; Sanz, N.; Hernandes, A.C.; Mastelaro, V.R. $Y_{0.9}Er_{0.1}Al_3(BO_3)_4$ Thin Films Preparedby the Polymeric Precursor Methodfor Integrated Optics. *J. Nanosci. Nanotechnol.* **2007**, *7*, 3629–3637, doi:10.1166/jnn.2007.811.
49. Maia, L.; Fick, J.; Bouchard, C.; Mastelaro, V.R.; Hernandes, A.; Ibáñez, A. Elaboration and optimization of (Y,Er)$Al_3(BO_3)_4$ glassy planar waveguides through the sol–gel process. *Opt. Mater.* **2010**, *32*, 484–490, doi:10.1016/j.optmat.2009.10.008.
50. Maia, L.; Fick, J.; Hernandes, A.; Mastelaro, V.R.; Ibáñez, A. Optical properties of amorphous, erbium-doped yttrium alumino-borate thin films. *Opt. Mater.* **2012**, *34*, 665–670, doi:10.1016/j.optmat.2011.09.014.

51. Malashkevich, G.E.; Sigaev, V.; Golubev, N.V.; Mamadzhanova, E.; Sukhodola, A.; Paleari, A.; Sarkisov, P.; Shimko, A.N. Spectroscopic properties of Sm-containing yttrium-aluminoborate glasses and analogous huntite-like polycrystals. *Mater. Chem. Phys.* **2012**, *137*, 48–54, doi:10.1016/j.matchemphys.2012.07.055.
52. Malashkevich, G.E.; Golubev, N.V.; Mamadzhanova, E.K.; Ziyatdinova, M.; Sigaev, V.N.; Sukhodola, A.A.; Khotchenkova, T.G.; Prusova, I.V.; Sergeev, I.I. Oxide glass with minimum distance 0.67 nm between rare-earth activators. *Glas. Ceram.* **2013**, *70*, 141–142, doi:10.1007/s10717-013-9527-4.
53. Ziyatdinova, M.; Golubev, N.V.; Ignat'Eva, E.; Okhrimchuk, A.; Khotchenkova, T.G.; Sigaev, V.N. Spectroscopic Properties of Yttrium-Aluminum-Borate Glasses Activated by Terbium and Cerium Ions. *Glas. Ceram.* **2016**, *72*, 366–369, doi:10.1007/s10717-016-9791-1.
54. Malashkevich, G.E.; Kouhar, V.; Pestryakov, E.; Sigaev, V.; Golubev, N.V.; Ziyatdinova, M.; Sukhodola, A. Spectral-luminescent and laser properties of the $(Y_{1-x},Yb_x)_2O_3$ $-Al_2O_3$ $-B_2O_3$ glasses. *Opt. Mater.* **2018**, *76*, 253–259, doi:10.1016/j.optmat.2017.12.042.
55. Naprasnikov, D.A.; Maltsev, V.V.; Leonyuk, N.I. $YAl_3(BO_3)_4$- and $GdAl_3(BO_3)_4$-based glass-ceramic composites. *Inorg. Mater.* **2015**, *52*, 68–75, doi:10.1134/s0020168515120092.
56. Naprasnikov, D.; Maltsev, V.V.; Leonyuk, N.; Gorbachenya, K.; Kurilchik, S.; Kisel, V.E.; Kuleshov, N. Micro-crystallization and spectroscopic properties of Er, Yb:RAl-borates (R = Y, Gd) obtained in $RAl_3(BO_3)_4$–$K_2Mo_3O_{10}$–B_2O_3–R_2O_3 and $RAl_3(BO_3)_4$–B_2O_3 systems. *J. Cryst. Growth* **2017**, *457*, 302–306, doi:10.1016/j.jcrysgro.2016.04.044.
57. Lorenzi, R.; Golubev, N.V.; Ziyatdinova, M.; Jarý, V.; Babin, V.; Malashkevich, G.E.; Paleari, A.; Sigaev, V.N.; Fasoli, M.; Nikl, M. Radio- and photoluminescence properties of Ce/Tb co-doped glasses with huntite-like composition. *Opt. Mater.* **2018**, *78*, 247–252, doi:10.1016/j.optmat.2018.02.016.